Chinese Chemical Letters 35 (2024) 109863

Contents lists available at ScienceDirect

Chinese Chemical Letters

journal homepage: www.elsevier.com/locate/cclet

Mn incorporated RuO_2 nanocrystals as an efficient and stable bifunctional electrocatalyst for oxygen evolution reaction and hydrogen evolution reaction in acid and alkaline

Jing Cao[a,b], Dezheng Zhang[a,b], Bianqing Ren[a,b], Ping Song[a,*], Weilin Xu[a,b,*]

[a] State Key Laboratory of Electroanalytical Chemistry, Changchun Institute of Applied Chemistry, Chinese Academy of Sciences, Changchun 130022, China
[b] University of Science and Technology of China, Hefei 230026, China

ARTICLE INFO

Article history:
Received 13 January 2024
Revised 3 April 2024
Accepted 6 April 2024
Available online 28 June 2024

Keywords:
RuO_2-based solid solution electrocatalysts
Oxygen evolution reaction
Hydrogen evolution reaction
Overall water splitting
Acid and alkaline

ABSTRACT

The development of efficient and stable bifunctional overall water-splitting is a crucial goal for clean and renewable energy, which is a challenging task. Herein, we report an Mn-incorporated RuO_2 (Mn-RuO_2) catalyst for highly efficient electrocatalytic oxygen evolution reaction (OER) and hydrogen evolution reaction (HER) in acid and alkaline media. Benefiting from a more electrochemical active area with the incorporation of Mn, the Mn-RuO_2 required an overpotential of 200 mV to attain a current density of 10 mA/cm^2 for OER in acid. DFT result indicates that the doping of Mn into RuO_2 can enhance the OER activity. An acidic overall water-splitting electrolyzer with good stability constructed by bifunctional Mn-RuO_2 only requires a cell voltage of 1.50 V to afford 10 mA/cm^2 and can operate stably for 50 h at 50 mA/cm^2, which is better than the state-of-the-art Ru-based catalyst. Additionally, the Mn-RuO_2 exhibits excellent HER and OER activity in alkaline media, and it shows superior activity and durability for overall water-splitting, only needing a cell voltage of 1.49 V to attain 10 mA/cm^2. The present work provides an efficient approach to designing and constructing efficient Ru-based electrocatalysts for overall water-splitting.

Due to the high demand for clean and renewable energy sources, electrochemical water spitting for (H_2) production is one of the most attractive and challenging tasks [1–3]. Furthermore, water electrolysis is one of the most efficient procedures for storing huge volumes of intermittently generated renewable electricity in the form of hydrogen gas [4–7]. However, an efficient electrocatalyst is necessary for large-scale applications owing to the slow reaction kinetics and complex electron transfer process [8–10]. To date, researchers have reported a number of catalysts for water-splitting reactions. For example, iridium (Ir) based electrocatalysts showed remarkable activity and stability toward oxygen evolution reaction (OER) [11–13], and platinum (Pt) based electrocatalysts are considered the best catalyst for hydrogen evolution reaction (HER) [14–16]. Although non-precious metal catalysts reported by some research teams have also played an important role, their activity or stability is still far behind that of noble metal-based catalysts in practical applications [17–19].

In practice, for proton exchange membrane (PEM) water electrolysis, conventional catalysts are based on iridium oxides because of the severe reaction environment on the OER side (low pH, high potential, and high O_2 concentration) [20,21]. Nonetheless, because Ir is one of the rarest elements on earth, the anode is not only the most inefficient component but also the primary cause of the electrolyzer's high cost [22,23]. The scarcity of Ir makes it difficult to meet the 2025 goal of the US Department of Energy (DOE) (H_2 production $<$ US $ 2/kg) [12,24]. Thus, designing advanced electrocatalysts with low or no Ir content is imperative [25]. Ruthenium (Ru) has been proven to possess suitable adsorption energies for H_{ads} and O_{ads}, which gives an opportunity to develop highly efficient HER and OER catalysts [26–28], and Ru with a lower price, higher earth abundance was regarded as a substitute for Ir [29]. Recently, Ru nanoparticles and mixed Ru oxide, such as $SrRuO_3$, $Cr_{0.6}Ru_{0.4}O_2$, Co-RuO_2, and Ni/Co-doped RuO_2 typically present good OER or HER activity, but poor solubility resistance of these Ru-based electrocatalysts under harsh anodic and acidic conditions, making it unrealistic for practical utilization due to the limited lifespan [30–33]. Therefore, the development of a highly active and stable bifunctional RuO_2-based electrocatalyst has been a challenge for overall water-splitting. In order

* Corresponding authors.
E-mail addresses: songping@ciac.ac.cn (P. Song), weilinxu@ciac.ac.cn (W. Xu).

https://doi.org/10.1016/j.cclet.2024.109863
1001-8417/

to resolve these problems, it was an effective strategy that the incorporation of other metal atoms into the RuO_2 could optimize the electronic structure to improve their activity and stability.

Based on the above-described results, herein, we developed high crystallinity RuO_2 catalysts with the incorporation of Mn, for use as a bifunctional electrocatalyst for OER and HER in acid and alkaline, presenting a high electrocatalytic activity and long-term stability. The strong electronic interaction between the incorporation of Mn and RuO_2 endows them with high OER and HER activity and stability. In an acid electrolyte, the overpotentials of OER and HER are only 200 mV and 20 mV at a current density of 10 mA/cm^2. Furthermore, the two-electrode PEM electrolyzer assembled by the Mn-RuO_2 requires a cell voltage as low as 1.50 V to achieve 10 mA/cm^2 for acid overall water-splitting as well as the long-term durability of 50 h at 50 mA/cm^2, which is superior to the state-of-the-art Ru-based catalyst. In addition, the Mn-RuO_2 exhibits low overpotentials of 37 and 220 mV for HER and OER in an alkaline electrolyte, the assembled alkaline electrolyzer similarly shows low cell voltages of 1.49 V at 10 mA/cm^2. These findings provide new insight into the development of highly efficient and stable catalysts for overall water-splitting in both alkaline and acidic electrolytes.

The synthesis process of Mn-RuO_2 is shown in Fig. 1a. Firstly, carbon-supported RuMn nanoparticles (RuMn/C) were obtained by thermal reduction of metal precursors adopted on a carbon black support at high temperatures under an H_2/Ar atmosphere (Fig. S1 in Supporting information). Carbon support during this process can effectively prevent nanoparticle agglomeration [34,35]. Subsequently, RuMn/C was ensured to fully oxidize to $RuMnO_x$, and to remove the carbon support. Finally, the unstable Mn species were removed by acid treatment to obtain the final catalysts Mn-RuO_2. The experimental details are provided in Supporting Information. As shown in Fig. 1b, X-ray diffraction (XRD) investigated the crystalline of these samples. The XRD pattern of the Mn-RuO_2 is well constant with the RuO_2 (JCPDS No. 40–1290) with good crystallinity [36], suggesting that the incorporation of Mn did not affect the RuO_2 lattice structure. Inductively Coupled Plasma Mass Spectrometry (ICP-MS) indicated the content of Mn and Ru in Mn-RuO_2 are 4 and 71.2 wt%. The morphological and structural details of RuMn/C, Mn-RuO_2, and RuO_2 were performed by transmission electron microscopy (TEM). The HADDF-STEM image of RuMn/C (Fig. 1c) shows its ultra-small size and the average of nanoparticles is 2.7 nm. Mn-RuO_2 nanoparticles were uniform in size, with an average diameter of about 6 nm, as shown in Fig. 1d, attributed to the alloy precursor's homogeneous particle size. Besides, the average size of RuO_2 nanoparticles is near 6 nm (Fig. S2 in Supporting information), indicating that the introduction of Mn essentially does not affect the size of RuO_2. Furthermore, the high-resolution TEM (HR-TEM) images (Fig. 1e) revealed that Mn-RuO_2 nanoparticles exhibited high crystallinity and distinct lattices. For the HR-TEM image of Mn-RuO_2, we observed crystalline structure with lattice fringe spacing of 0.317 nm and 0.252 nm, which can be ascribed to the (110) and (101) lattice planes of RuO_2. From the HR-TEM image of as-prepared RuO_2 (Fig. 1f), we also observed its high crystallinity and distinct lattices like Mn-RuO_2, and the lattice fringe spacing of the same lattice planes did not change. Energy-dispersive spectroscopic (EDS) elemental mapping (Fig. 1g) showed the homogeneous distribution of Mn, Ru, and O elements across the nanoparticles. These results confirmed Mn atoms were successfully incorporated into RuO_2.

To understand the electronic structure of Mn-RuO_2, the surface compositions and chemical states were investigated by X-ray photoelectron spectroscopy (XPS) measurements. The full-scan XPS survey spectrum verifies the expected elements of Mn, Ru, and O in Mn-RuO_2 nanoparticles (Fig. S3 in Supporting information), and revealed an Mn atomic ratio of 3.22 at% (Mn:Ru ratio ~1:10) in Mn-RuO_2. In the high-resolution Mn 2p XPS spectrum (Fig. 2a), two peaks at 652.0 eV and 641.3 eV were assigned to Mn $2p_{1/2}$ and

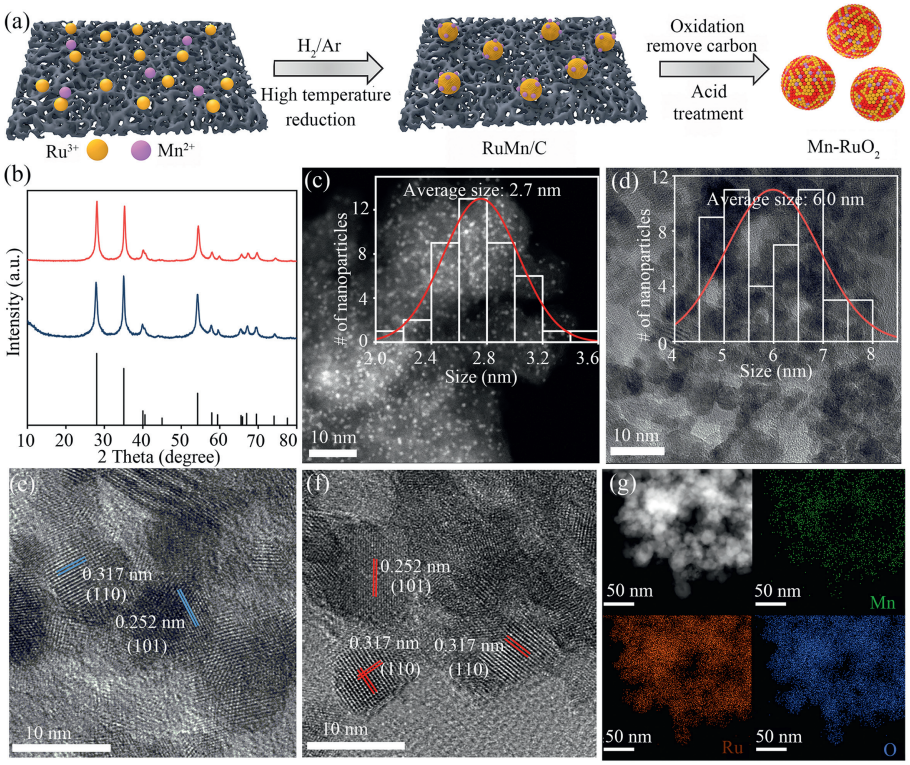

Fig. 1. (a) Schematic illustration of the synthesis of Mn-RuO_2. (b) XRD patterns of Mn-RuO_2 and RuO_2. (c) STEM images of RuMn/C. (d) TEM images of Mn-RuO_2. Inset is the size distribution of the correlation nanoparticles. HR-TEM images of Mn-RuO_2 (e) and RuO_2 (f). (g) STEM image and EDX elemental mapping of Mn-RuO_2.

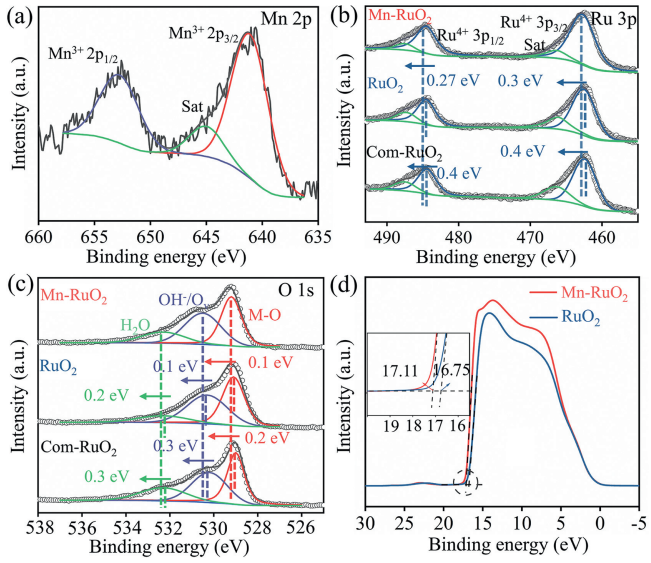

Fig. 2. (a) The XPS spectra of Mn 2p of Mn-RuO_2. The XPS spectra of Ru 3p (b), O 1s (c) of Mn-RuO_2, RuO_2, and Com-RuO_2. (d) The UPS spectra of Mn-RuO_2 and RuO_2. Inset is the $E_{cut\ off}$ of Mn-RuO_2 and RuO_2.

Mn $2p_{3/2}$ of Mn^{3+}, respectively [37,38]. Owing to Ru $3d_{3/2}$ regions inherently overlapping with the C 1s spectra (Fig. S4 in Supporting information), the Ru 3p spectrum was examined for the oxidation state of Ru. For the Ru 3p XPS spectrum (Fig. 2b), two sets of doublet peaks located at 462.9 eV and 484.6 eV with two satellite peaks, can be attributed to Ru^{4+} [39–42]. The binding energy of Ru $3p_{3/2}$ for Mn-RuO_2 had a positive shift (0.3 eV and 0.4 eV) in contrast to as-prepared RuO_2 and commercial RuO_2 (Com-RuO_2), indicating exits the strong electronic interaction between the incorporation of Mn and RuO_2. In addition, the peaks of Ru^{4+} $3p_{3/2}$ with higher binding energy possibly suggested $Ru^{>4+}$ species exiting [30]. Based on previous studies, Ru species with a high valance can enhance the OER activity [43]. In the O 1s spectrum of Mn-RuO_2 (Fig. 2c), the peaks the peaks located at about 529.2 eV, 530.5 eV, and 532.3 eV were ascribed to M-O (lattice oxygen), OH^-/oxygen vacancy, and absorbed H_2O [44,45]. For Mn-RuO_2, the three peaks display a positive shift to higher binding energy, indicating that O grabs fewer electrons from the metal elements with doping Mn atoms. Furthermore, we employed ultraviolet photoemission spectroscopy (UPS) to investigate the energy level differences between Mn-RuO_2 and RuO_2 (Fig. 2d). Since the secondary electron cut-off edges for Mn-RuO_2 and RuO_2 are 17.11 eV and 16.75 eV, the values of work function for Mn-RuO_2 and RuO_2 are 4.11 eV and 4.47 eV. From a fundamental point of view, the materials' work function is an effective parameter that characterizes their electron donation ability. Mn-RuO_2 with the lower work function suggested the smaller energy barrier of electron transfer from the surface of electrocatalysts to reactants and intermediates, accelerating the HER and OER processes [46–48].

The OER performance of Mn-RuO_2 and contrast catalysts are investigated by a three-electrode system in 0.5 mol/L H_2SO_4. As shown in Fig. 3a, linear sweep voltammetry (LSV) curves showed that as-prepared RuO_2 exhibits better OER activity compared to Com-RuO_2, and delivers low overpotentials of 210 mV to achieve 10 mA/cm^2. For Mn-RuO_2, the incorporation of Mn showed an obvious enhancement in the OER activity of as-prepared RuO_2 and the overpotentials of 200 mV to achieve 10 mA/cm^2 (Fig. 3b). Besides RuO_2 and Com-RuO_2, Mn-RuO_2 also showed higher OER activity than its precursors RuMn/C (Fig. S5 in Supporting information) and $MnRuO_x$ (Fig. S6 in Supporting information). The OER performance as a function of Ru amounts was calculated. Among them (Fig. 3c), Mn-RuO_2 delivered the highest mass activity of 956 A g/Ru, which is about 9.5-fold higher than that of Com-RuO_2 (103 A g/Ru), revealing the superior utilization of Ru in Mn-RuO_2. After adjusting the molar ratios of Mn and Ru (Fig. S7 in Supporting information) and oxidation temperature (Fig. S8 in Supporting information), the Mn-RuO_2 (Mn: 4 wt%, oxidation temperature: 500 °C) catalysts displayed the highest OER catalytic activity. In addition, the Tafel slope of Mn-RuO_2 was as low as 56.1 mV/dec (Fig. 3d), which was lower than that of as-prepared RuO_2 (69.1 mV/dec) and Com-RuO_2 (99.2 mV/dec), implying a much more rapid kinetic process in Ru sites after regulating the electronic structures of RuO_2 by introducing Mn atoms. Similarly, electrochemical impedance spectroscopy (EIS) of Mn-RuO_2 showed the lowest charge transfer resistance in comparison with RuO_2 and Com-RuO_2 (Fig. 3e), indicating a higher reaction rate, and faster charge transfer [49]. To better understand the origin of the high OER performance of Mn-RuO_2, the double-layer capacitance (C_{dl}) and electrochemically active surface area (ECSA) were also calculated by cyclic voltammetry (CV) measurements (Fig. 3f). The Mn-RuO_2 catalysts had the highest C_{dl} and ECSA (Fig. S9 in Supporting information), which was 2-fold higher than RuO_2 and 10.7-fold higher than Com-RuO_2, suggesting a more electrochemical active surface area to expose abundant active sites with the incorporation of Mn. The activity and kinetics of Mn-RuO_2 were compared with those of recently reported Ru-based catalysts, suggesting that Mn-RuO_2 possesses better activity and faster OER kinetics than most of the reported Ru-based catalysts (Fig. 3g and Table S1 in Supporting information). Furthermore, Fe, Co, and Ni doping also had an identical effect that can enhance the activity of RuO_2 (Fig. S10 in Supporting information). In addition to the high activity, stability is a critical indicator for evaluating the OER performance in an acid medium. We investigated OER durability at 10 mA/cm^2 in 0.5 mol/L H_2SO_4 (Fig. 3h). The stability of current state-of-the-art noble RuO_2 catalysts is still a major concern because they quickly form acidic soluble RuO_4 species with higher oxidation states in highly oxidative and acidic environments [50,51]. Indeed, our result confirmed that the Com-RuO_2 catalyst suffers from fast performance decay with quickly elevated potentials within a few hours. Impressively, the catalytic stability of Mn-RuO_2 is far greater than that of commercial RuO_2. As a result, Mn-RuO_2 could continuously catalyze the OER for 100 h and only decay 30 mV. Furthermore, we systematically characterized post-catalysis Mn-RuO_2. HR-TEM (Fig. S11 in Supporting information) and XRD (Fig. S12 in Supporting information) results after the durability show structures of catalysts were retained well and no distinct structure reconstruction. The above results indicate the addition of Mn atoms can effectively improve the activity and stability of RuO_2 in acid electrolytes.

To further confirm the different catalytic performances, we explore the OER mechanism on various catalysts by performing DFT calculations. Our TEM observations indicated that the (110) facet was the most exposed facet for RuO_2 and Mn-RuO_2. Therefore, the slab (110) surface models of Mn-RuO_2 and RuO_2 were constructed to simulate the catalysts obtained in the experiment (Fig. S13 in Supporting information). Fig. 4a showed the Ru-O bond length of Mn-RuO_2 and RuO_2, indicating the doping of Mn evoked longer Ru-O bond length in favor of OER activity. Meanwhile, the free energy of OER with consecutive coupled proton-electron transfer steps was calculated to evaluate the OER performance for RuO_2 and doped Mn-RuO_2 with the adsorbate evolution mechanism (AEM, Fig. 4b). The formation of *OOH was found to be the rate-determining step (RDS) for the two catalysts, and the Mn-RuO_2 exhibited a lower free energy barrier compared with the RuO_2, which showed a smaller overpotential by 440 mV (Fig. 4c). DFT result indicates that the doping of Mn into RuO_2 can enhance the OER activity in acid media.

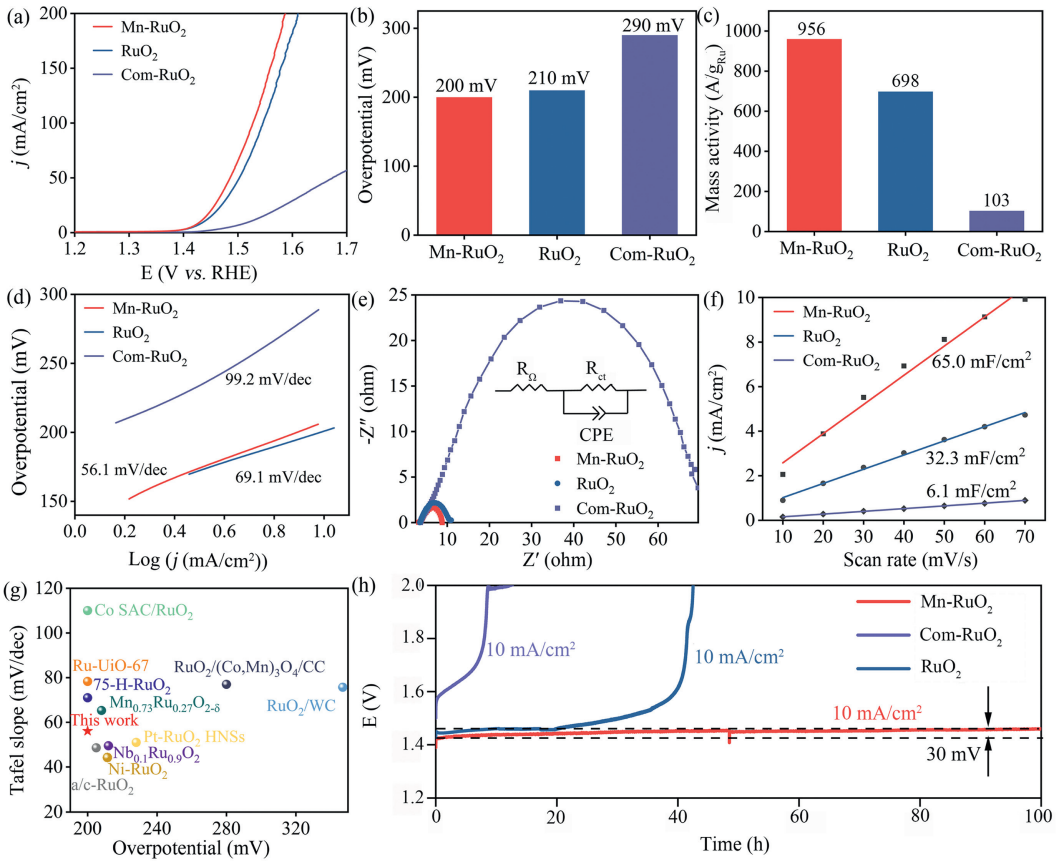

Fig. 3. OER performance evaluations in 0.5 mol/L H_2SO_4: (a) polarization curves, (b) the overpotentials at 10 mA/cm^2, (c) the mass activity at 1.55 V (*vs.* RHE), (d) the corresponding Tafel plots of Mn-RuO_2, RuO_2, and Com-RuO_2. (e) Nyquist plots of Mn-RuO_2, RuO_2, and Com-RuO_2. Inset is the equivalent circuit. (f) C_{dl} plots of Mn-RuO_2, RuO_2, and Com-RuO_2. (g) Comparison of overpotential and Tafel slope between Mn-RuO_2 and recently reported Ru-based OER electrocatalysts. (h) Long-term stability of Mn-RuO_2, RuO_2, and Com-RuO_2 at 10 mA/cm^2 in 0.5 mol/L H_2SO_4.

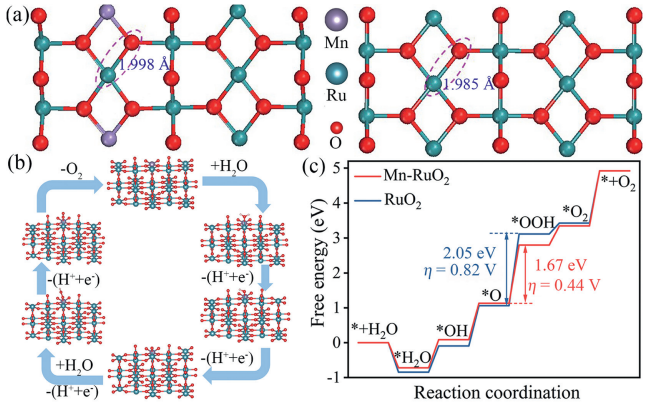

Fig. 4. (a) The local active site structure for Mn-RuO_2 (left) and RuO_2 (right) with corresponding Ru-O bond lengths. (b) Structures of reaction intermediates for OER on Mn-RuO_2 (110) surface. (c) The free energy diagram for OER at 0 V on Mn-RuO_2 and RuO_2 catalysts.

In general, RuO_2 has lower HER activity under acidic conditions. However, besides the outstanding OER catalytic performance, Mn-RuO_2 can also exhibit superior HER performances in acid media. As shown in Fig. 5a, although the activity is not as good as commercial Pt/C (Com-Pt/C), Mn-RuO_2 displays excellent HER performance with a lower overpotential of 20 mV at 10 mA/cm^2, much smaller than that of RuO_2 (48 mV) and Com-RuO_2 (167 mV, Fig. 5b). Moreover, the Tafel slope is only 25.5 mV/dec for Mn-RuO_2 much lower than that of as-prepared RuO_2 and Com-RuO_2 (Fig. 5c), and it has the lowest charge transfer resistance (Fig. S14 in Supporting information), indicating the superior reaction kinetics process of Mn-RuO_2 for HER. Encouraged by the superior OER and HER activity of Mn-RuO_2, a two-electrode PEM configuration was constructed by utilizing the bifunctional Mn-RuO_2 as both the cathode and the anode in acidic media (Mn-RuO_2//Mn-RuO_2). For comparison, the electrolyzers are based on commercial 20 wt% Pt/C and commercial RuO_2 (Pt/C//Com-RuO_2), commercial 20 wt% Pt/C and as-prepared RuO_2 (Pt/C//RuO_2) as references. Notably, the Mn-RuO_2//Mn-RuO_2 displayed excellent activity toward overall water-splitting in acid electrolytes and the electrolyzer's potentials were only required 1.50 V and 1.56 V at 10 and 50 mA/cm^2, respectively (Fig. 5d). However, to attach such current density, the cell potentials were 1.54 V and 1.59 V for Pt/C//RuO_2, 1.63 V and 1.71 V for Pt/C//Com-RuO_2, respectively. Additionally, the long-term stability of Mn-RuO_2//Mn-RuO_2 for overall water-splitting was explored by chronopotentiometry tests at 50 mA/cm^2 (Fig. 5e). The Mn-RuO_2//Mn-RuO_2 electrolyzer exhibited superior durability and can operate stably for 50 h with only a decay of 30 mV. In particular, we measured the Faradaic efficiency of Mn-RuO_2//Mn-RuO_2 electrolyzer for H_2 and O_2 evolution (Fig. S15 in Supporting information) in acid, the measured amount of O_2 and H_2 varies with time at a given current (50 mA); the molar ratio of H_2 and O_2 is close to 2:1. As a result, the final Faradaic efficiency of cathode and anode is both around 99%. The activity and stability of Mn-RuO_2//Mn-RuO_2 were better than other reported bifunctional electrocatalysts for overall water-splitting in acid (Table S2 in Supporting information). These results indicate the high potential of the Mn-RuO_2 catalyst for acid overall water electrolysis.

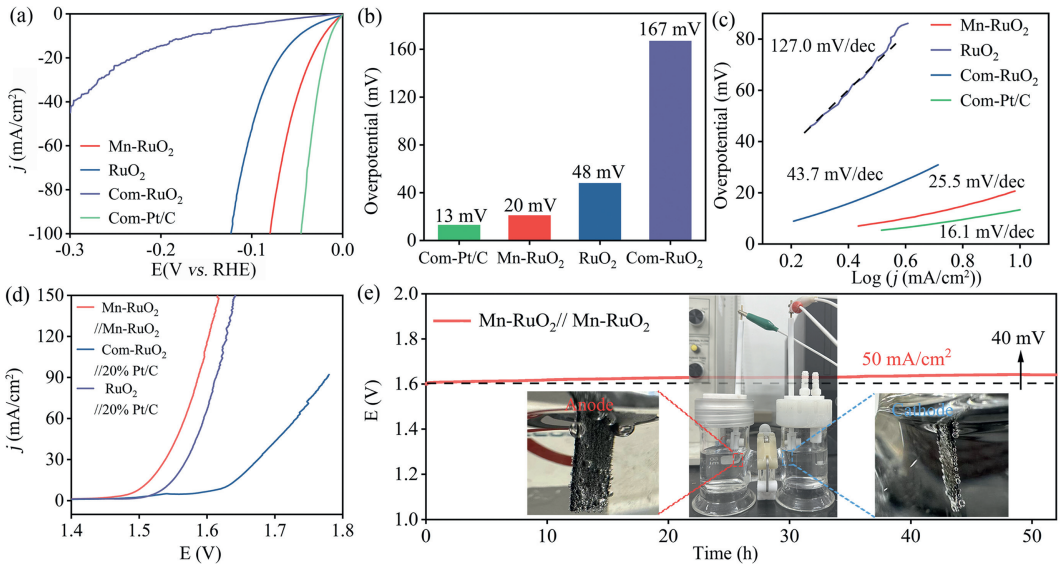

Fig. 5. HER and overall water-splitting performance evaluations in 0.5 mol/L H_2SO_4: (a) HER polarization curves, (b) the overpotentials at 10 mA/cm^2, and (c) the corresponding Tafel plots of Mn-RuO_2, RuO_2, Com-RuO_2, and Com-Pt/C. (d) Polarization curves of Mn-RuO_2//Mn-RuO_2 and reference for overall water-splitting. (e) Chronopotentiometry tests of Mn-RuO_2//Mn-RuO_2 at 50 mA/cm^2. The inset of (e) shows a digital photograph of the two-electrode PEM electrolyzer with H_2 and O_2 evolving at the cathode and anode, respectively.

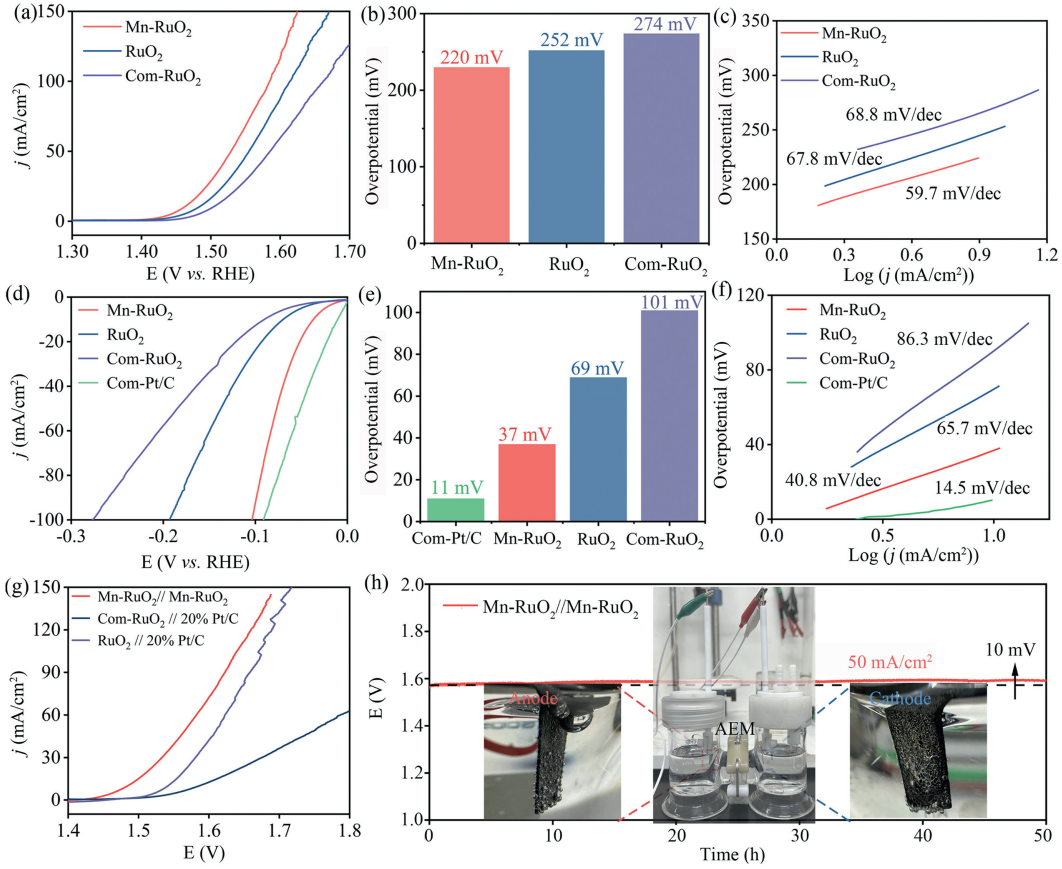

Fig. 6. OER, HER, and overall water-splitting performance evaluations in 1 mol/L KOH: (a) OER, (d) HER polarization curves, (b, e) the overpotentials at 10 mA/cm^2, and (c, f) the corresponding Tafel plots of Mn-RuO_2, RuO_2, Com-RuO_2 and Com-Pt/C. (g) Polarization curves of Mn-RuO_2//Mn-RuO_2 and reference for overall water-splitting. (h) Chronopotentiometry tests of Mn-RuO_2//Mn-RuO_2 at 50 mA/cm^2. The inset of (h) shows a digital photograph of the two-electrode AEM electrolyzer with H_2 and O_2 evolving at the cathode and anode, respectively.

Based on the high HER and OER activity of Mn-RuO_2 in acid, we further evaluated Mn-RuO_2 electrocatalytic performance toward HER, OER, and overall water-splitting in alkaline electrolytes. As shown in Fig. 6a, the Mn-RuO_2 showed excellent OER activity in 1.0 mol/L KOH with an overpotential of 220 mV to deliver 10 mA/cm^2, in contrast to the RuO_2 (252 mV) and Com-RuO_2 (274 mV, Fig. 6b). Additionally, Mn-RuO_2 possesses the fastest electrocatalytic kinetics with the smallest Tafel slope of 59.7 mV/dec (Fig. 6c) and charge-transfer resistances (Fig. S16 in Supporting information). Meanwhile, as shown in Fig. 6d, the Mn-RuO_2 exhibited a much lower HER overpotential of 37 mV at 10 mA/cm^2, which was superior to that of the RuO_2 (69 mV) and Com-RuO_2 (101 mV, Fig. 6e). Furthermore, the kinetic process was revealed by the Tafel slope and EIS. The Mn-RuO_2 showed the lowest Tafel slope (40.8 mV/dec, Fig. 6f) and the smallest charge-transfer resistances (Fig. S17 in Supporting information) compared to RuO_2 and Com-RuO_2. To better understand the origin of the high OER and HER performance of Mn-RuO_2, we employed CV measurements calculated to the C_{dl} and ECSA (Fig. S18 in Supporting information), Mn-RuO_2 exhibited a considerably high C_{dl} value of 43.2 mF/cm^2, which corresponds to an ECSA value of 1234.2 cm^2 (Fig. S19 in Supporting information), was 3-fold higher than RuO_2 and 7-fold higher than Com-RuO_2, indicating Mn-RuO_2 also exposed a more electrochemical active surface area in alkaline electrolytes compared to other catalysts. Because of the significant HER and OER activity in 1.0 mol/L KOH, the overall water-splitting activity of the Mn-RuO_2 catalyst was evaluated with a two-electrode configuration. As shown in Fig. 6g, the Mn-RuO_2//Mn-RuO_2 showed overall water-splitting superior activity, only needing 1.48 V and 1.56 V at 10 and 50 mA/cm^2, respectively, which was much lower than the references Pt/C//Com-RuO_2 (1.58 V and 1.75 V) and Pt/C//RuO_2 (1.54 V and 1.61 V) at the same current densities. Impressively, the overall water-splitting activity of Mn-RuO_2//Mn-RuO_2 was higher than most of the recently reported electrocatalysts for overall water-splitting in alkaline (Table S3 in Supporting information). We measured the Faradaic efficiency of Mn-RuO_2//Mn-RuO_2 electrolyzer for H_2 and O_2 evolution (Fig. S20 in Supporting information) in alkaline, the molar ratio of H_2 and O_2 is close to 2:1. And the final Faradaic efficiency is both around 99%. Correspondingly, Mn-RuO_2//Mn-RuO_2 can deliver superior durability even with the reaction time prolonging to 50 h at 50 mA/cm^2 with only decay of 10 mV (Fig. 6h). The above results indicate that Mn-RuO_2 can be one of the most promising Ru-based catalysts for practical alkaline water electrolysis.

In summary, Mn-RuO_2 nanocrystals are successfully synthesized as bifunctional electrocatalysts for overall water-splitting in acid and alkaline. The as-prepared Mn-RuO_2 catalysts show excellent OER activity in acid electrolytes, resulting in an overpotential of 200 mV at 10 mA/cm^2, which outperforms most Ru-based catalysts. DFT result indicates that the doping of Mn into RuO_2 can enhance the OER activity. Meanwhile, the Mn-RuO_2 also possesses outstanding HER activity, leading to an overpotential of 20 mV at 10 mA/cm^2. Furthermore, the two-electrode PEM electrolyzer assembled by the Mn-RuO_2, yielding 10 mA/cm^2 at 1.5 V and the long-term durability of 50 h at 50 mA/cm^2, which is superior to the state-of-the-art Ru-based catalyst. In addition, the Mn-RuO_2 also exhibits high activity for HER and OER in alkaline media, and the assembled alkaline electrolyzer by Mn-RuO_2 shows low cell voltages of 1.49 V at 10 mA/cm^2. Such remarkable performance of the Mn-RuO_2 was attributed to the incorporation of Mn modulating the electronic structure of RuO_2, exposing more electrochemically active areas, and accelerating HER and OER processes. This work provides an effective strategy for designing highly active and stable Ru oxides-based electrocatalysts toward OER and HER in acid and alkaline.

Declaration of competing interest

The authors declare that they have no known competing financial interests or personal relationships that could have appeared to influence the work reported in this paper.

CRediT authorship contribution statement

Jing Cao: Conceptualization, Data curation, Formal analysis, Investigation, Software, Supervision, Validation, Writing – original draft, Writing – review & editing. **Dezheng Zhang:** Software. **Bianqing Ren:** Investigation. **Ping Song:** Investigation, Software, Writing – review & editing. **Weilin Xu:** Conceptualization, Funding acquisition, Writing – review & editing.

Acknowledgments

This work was supported by the Key Research and Development Program sponsored by the Ministry of Science and Technology (MOST, Nos. 2022YFB4002000, 2022YFA1203400) and the National Natural Science Foundation of China (Nos. 21925205, 22072145, 22372155, 22005294 and 22102172).

Supplementary materials

Supplementary material associated with this article can be found, in the online version, at doi:10.1016/j.cclet.2024.109863.

References

[1] S. Chu, A. Majumdar, Nature 488 (2012) 294–303.
[2] Q. Shi, C. Zhu, D. Du, Y. Lin, Chem. Soc. Rev. 48 (2019) 3181–3192.
[3] A. Vojvodic, J.K. Norskov, Science 334 (2011) 1355–1356.
[4] M.F. Lagadec, A. Grimaud, Nat. Mater. 19 (2020) 1140–1150.
[5] Y. Zang, S. Niu, Y. Wu, et al., Nat. Commun. 10 (2019) 1217.
[6] Y. Wu, X. Liu, D. Han, et al., Nat. Commun. 9 (2018) 1425.
[7] X. Wang, G. Huang, Z. Pan, et al., Chem. Eng. J. 428 (2022) 131190.
[8] F. Chen, Z. Zhang, W. Liang, et al., Chin. Chem. Lett. 33 (2022) 1395–1402.
[9] S.N. Hussain, Y. Men, Z. Li, et al., Chin. Chem. Lett. 34 (2023) 107364.
[10] W. Wu, Y. Huang, X. Wang, P.K. Shen, J. Zhu, Chem. Eng. J. 469 (2023) 143879.
[11] J. Cao, T. Mou, B. Mei, et al., Angew. Chem. Int. Ed. 62 (2023) e202310973.
[12] S. Hao, H. Sheng, M. Liu, et al., Nat. Nanotechnol. 16 (2021) 1371–1376.
[13] X.Q. Wang, X.Y. Ma, W.Z. Wu, et al., Rare Metals 43 (2024) 1977–1988.
[14] G. Chen, W. Chen, R. Lu, et al., J. Am. Chem. Soc. 145 (2023) 22069–22078.
[15] Z. Wu, P. Yang, Q. Li, et al., Angew. Chem. Int. Ed. 62 (2023) e20230040.
[16] F. Luo, Y. Yu, X. Long, et al., J. Colloid Interface Sci. 656 (2024) 450–456.
[17] Y. Sun, X. Li, T. Zhang, et al., Angew. Chem. Int. Ed. 60 (2021) 21575–21582.
[18] A. Li, S. Kong, C. Guo, et al., Nat. Catal. 5 (2022) 109–118.
[19] Y. Zhang, K. Dastafkan, Q. Zhao, et al., Appl. Catal. B 341 (2024) 123297.
[20] F.Y. Chen, Z.Y. Wu, Z. Adler, H. Wang, Joule 5 (2021) 1704–1731.
[21] C. Spoeri, J.T.H. Kwan, A. Bonakdarpour, D.P. Wilkinson, P. Strasser, Angew. Chem. Int. Ed. 56 (2017) 5994–6021.
[22] D.A. Kuznetsov, M.A. Naeem, P.V. Kumar, et al., J. Am. Chem. Soc. 142 (2020) 7883–7888.
[23] N. Li, L. Cai, C. Wang, et al., J. Am. Chem. Soc. 143 (2021) 18001–18009.
[24] Z. Shi, J. Li, Y. Wang, et al., Nat. Commun. 14 (2023) 843.
[25] F. Luo, S. Pan, Y. Xie, et al., Adv. Sci. 10 (2023) 2305058.
[26] L. Hou, Z. Li, H. Jang, et al., Adv. Energy Mater. 13 (2023) 2300177.
[27] C. Wang, L. Qi, Angew. Chem. Int. Ed. 59 (2020) 17219–17224.
[28] F. Luo, S. Pan, Y. Xie, et al., J. Energy Chem. 90 (2024) 1–6.
[29] Y. Yao, S. Hu, W. Chen, et al., Nat. Catal. 2 (2019) 304–313.
[30] Y. Lin, Z. Tian, L. Zhang, et al., Nat. Commun. 10 (2019) 162.
[31] J. Wang, Y. Ji, R. Yin, et al., J. Mater. Chem. A 7 (2019) 6411–6416.
[32] S.H. Chang, N. Danilovic, K.C. Chang, et al., Nat. Commun. 5 (2014) 4191.
[33] K. Shah, R. Dai, M. Mateen, et al., Angew. Chem. Int. Ed. 61 (2022) e202114951.
[34] S.L. Xu, S.C. Shen, W. Xiong, et al., Inorg. Chem. 59 (2020) 15953–15961.
[35] Z.Y. Wu, F.Y. Chen, B. Lie, et al., Nat. Mater. 22 (2023) 100–108.
[36] J. Wang, C. Cheng, Q. Yuan, et al., Chem 8 (2022) 1673–1687.
[37] V. Dicastro, G. Polzonetti, J. Electron Spectrosc. Relat. Phenom. 48 (1989) 117–123.
[38] X. Feng, D.F. Cox, Surf. Sci. 675 (2018) 47–53.
[39] C. Peng, W. Zhao, Z. Li, et al., Chem. Eng. J. 425 (2021) 131707.
[40] S.H. Ji, N.R. Chodankar, D.H. Kim, Electrochim. Acta 325 (2019) 134879.
[41] H. Zhu, Y. Wang, Z. Jiang, B. Deng, Z.J. Jiang, J. Mater. Chem. A (2023) 25252–25261.
[42] N. Cong, Y. Han, L. Tan, et al., J. Electroanal. Chem. 881 (2021) 114955.

[43] K. Wang, Y. Wang, B. Yang, et al., Energy Environ. Sci. 15 (2022) 2356–2365.
[44] J. He, W. Li, P. Xu, J. Sun, Appl. Catal. B 298 (2021) 12508.
[45] Y. Li, P. Zhang, J. Xiong, et al., Environ. Sci. Technol. 55 (2021) 16153–16162.
[46] Y. Duan, Z.Y. Yu, L. Yang, et al., Nat. Commun. 11 (2020) 4789.
[47] Q. Hu, K. Gao, X. Wang, et al., Nat. Commun. 13 (2022) 3958.
[48] L. Fu, J. Zhou, L. Zhou, et al., Chem. Eng. J. 418 (2021) 129422.
[49] Z.L. Zhao, Q. Wang, X. Huang, et al., Energy Environ. Sci. 13 (2020) 5143–5151.
[50] T. Reier, M. Oezaslan, P. Strasser, ACS Catal. 2 (2012) 1765–1772.
[51] W. Zhu, F. Yao, K. Cheng, et al., J. Am. Chem. Soc. 145 (2023) 17995–18006.